

Article

Axial Impact Resistance of High-Strength Engineering Geopolymer Composites: Effect of Polyethylene Fiber Content and Strain Rate

Yu Ling ¹, Xiafei Zhang ¹, Weiyu Zou ¹, Chang Feng ², Huaming Lai ², Jialin Yang ³ and Beixin Xie ^{2,*}

¹ Guangzhou Power Supply Bureau, Guangdong Power Grid Co., Ltd., China Southern Power Grid Co., Ltd., Guangzhou 510006, China; 15915714058@163.com (Y.L.); 18102278577@189.cn (X.Z.); wyw1400@163.com (W.Z.)

² School of Civil and Transportation Engineering, Guangdong University of Technology, Guangzhou 510006, China; 13016603278@163.com (C.F.); 18200662652@163.com (H.L.)

³ School of Civil Engineering, Central South University, Changsha 410075, China; yangjialinchn@foxmail.com

* Correspondence: 13mars@163.com

Abstract: High-strength engineered geopolymer composite (EGC) materials exhibit excellent mechanical properties under quasistatic loading, thus showing great potential in military and civilian facilities subjected to impact or explosive loading. However, its dynamic mechanical response under high-speed loading is not fully understood. In this study, dynamic compressive test was performed on EGC with PE fiber contents of 0%, 0.5%, 1.0%, 1.5%, and 2.0% using the Split Hopkinson Pressure Bar (SHPB) test. The results indicated that EGC reinforced with 1.5% fiber exhibited optimal static and dynamic mechanical performance. In the strain rate range of 181 s⁻¹ to 201 s⁻¹, when the fiber content increased from 1.0% to 1.5% and 2.0%, the dynamic compressive strength of the EGC increased by 24.3%, 28.8%, and 44.0%, respectively, compared to the matrix without fiber. Dynamic parameters of the EGC, including dynamic compressive strength, dynamic increase factor, and impact toughness, showed sensitivity to strain rates and increased with strain rate. A modified model, incorporating the fiber bridging effect, was proposed based on the CEB-FIP model, providing important guidance for practical engineering applications.

Keywords: dynamic compressive behavior; EGC; fiber content; SHPB



Citation: Ling, Y.; Zhang, X.; Zou, W.; Feng, C.; Lai, H.; Yang, J.; Xie, B. Axial Impact Resistance of High-Strength Engineering Geopolymer Composites: Effect of Polyethylene Fiber Content and Strain Rate. *Buildings* **2024**, *14*, 1438. <https://doi.org/10.3390/buildings14051438>

Academic Editor: Flávio De Andrade Silva

Received: 20 March 2024

Revised: 8 May 2024

Accepted: 10 May 2024

Published: 16 May 2024



Copyright: © 2024 by the authors. Licensee MDPI, Basel, Switzerland. This article is an open access article distributed under the terms and conditions of the Creative Commons Attribution (CC BY) license (<https://creativecommons.org/licenses/by/4.0/>).

1. Introduction

In 2001, the terrorist incident of planes crashing into the Twin Towers in New York and the impact loading that was encountered during the service of the infrastructure (e.g., explosions, impacts, etc.) aroused great interest in building materials with excellent impact resistance. Traditional concrete has poor tensile properties and is brittle, which is often disastrous when subjected to impact loading. Fiber-reinforced concrete (FRC) has significantly improved tensile strength, fracture toughness, and fracture modes by adding discrete short fiber to the concrete [1–3]. Engineered cementitious composites (ECCs) have garnered attention for their outstanding crack tolerance and superior tensile strength, with the behavior of multiple cracks expanding being widely studied [4–7]. However, conventional ECCs tend to be high in cement, which has been the main cause of high CO₂ emissions in the construction sector, and its greenness is a concern [8,9]. The use of geopolymer as a novel binding material is considered a significant breakthrough in the construction industry to reduce the carbon footprint. Geopolymer-utilized industrial by-products, such as fly ash (FA), ground granulated blast furnace slag (GGBS), and metakaolin as precursors, react with alkaline activators (such as sodium hydroxide and sodium silicate solutions) to form a reaction [10,11]. These activators dissolve the silicate and aluminate components in the precursors, thus initiating a polymerization reaction that ultimately produces an amorphous gel. Previous studies demonstrated that geopolymer concrete

exhibited excellent early strength and durability, thus making it a promising material to replace traditional Portland cement concrete [12,13]. The engineering geopolymer composite (EGC) is a low-carbon composite made of geopolymer gel, various aggregates, and short fiber [14–18]. The EGC, similar to the ECC, also has excellent tensile properties, with tensile strengths of up to 10 MPa and tensile strains of up to 3–22%, which are accompanied by strain-hardening behaviors and multiseam spreading and have attracted a great deal of interest from researchers [17,19–21].

In the developed EGC, FA or GGBS materials have been commonly used as precursors, while a blend of sodium hydroxide (SH) solution and sodium silicate (SS) solution acts as the alkali activator [22–24]. FA is widely available globally and exhibits good processability. However, an FA-based EGC often requires high-temperature curing conditions to achieve the desired mechanical performance [25]. GGBS, with a higher calcium content, could substitute for a portion of the FA, thereby accelerating the early reaction rate and enhancing early strength and making it suitable for actual engineering curing conditions [25,26]. In previous studies on slag–fly ash-based EGCs, researchers have investigated the influence of variables such as the type of slag/fly ash ratio, the dosage of the alkali activator, the sand-to-binder ratio, the type of fiber, the fiber content, and the fiber length on both the workability and mechanical properties of the fresh paste [16,26–29]. For example, Lee et al. [30] and Choi et al. [22] achieved a mortar matrix with appropriate viscosity by adjusting the ratio of water to binder and the type of reducing activator. Suitable viscosity promotes the uniform dispersion of high aspect ratio fiber, thereby resulting in an EGC with a tensile strength of 13.06 MPa and a tensile strain of 7.5%. In terms of the fiber type, most of the studies used oiled polyvinyl alcohol (PVA) fiber and ultra-high molecular weight polyethylene fiber (UHMPE). PVA fiber has excellent fiber/matrix interfacial properties and has been one of the first fibers to be used in highly ductile composites (ECC/EGC), and PE fiber has also been used by a wide range of researchers as a result of its excellent tensile properties. The fiber content plays a pivotal role in determining the mechanical response of highly ductile composite materials (ECC/EGC). Ahmed and Ronnie et al. [31] explored the impact of fiber content (ranging from 0.5% to 2%) on the uniaxial tensile and three-point bending performance of EGCs. The results revealed that the optimal fiber volume fraction was 1%, at which the material exhibited excellent tensile strain and flexural hardening behavior. However, as the volume fraction of PE fiber increased, the compressive strength of the composite gradually decreased. Moreover, it was found that with higher PE volume fractions, the crack density in the EGC increases, thereby leading to a higher strain capacity [32].

For the dynamic mechanical properties of the EGC, it has been shown that regardless of precursor type and whether subjected to heat curing, the EGC's dynamic compressive strength exhibits significant strain rate sensitivity [17,33–35]. Furthermore, the fiber length, fiber volume fraction, and fiber distribution were closely associated with the EGC's performance under high-speed loading conditions [36,37]. The dynamic compressive response of PVA–EGC at different fiber volume fractions (0%, 1%, 1.5%, and 2%) was studied, with the volume fraction of 1.5% identified as the optimal choice for considering both quasistatic and dynamic behavior, as per Wang et al. [36]. Zhong et al. [38] conducted dynamic splitting tensile and dynamic compressive tests using recycled fiber instead of PVA fiber. Materials mixed with 0.25% recycled polymer and 1.75% PVA fiber demonstrated improved quasistatic performance and dynamic compressive response according to the results [38,39]. Compared to the ECC, when the same PVA fiber was used, the EGC's ability to dissipate impact energy was 1.6 times that of the ECC. When the environmental temperature reached 100 °C, both the maximum impact load and duration of impact of the EGC were higher than the ECC. Therefore, the EGC was found to be more suitable for protective buildings in sub-high-temperature environments [40,41]. Additionally, under both quasistatic and dynamic tensile loading, the PE–EGC exhibited superior mechanical performance compared to the PVA–EGC [17].

However, to date, research on the mechanical response of PE–EGC under high strain rates has been limited. It is worth noting, particularly, the difference in wettability between PVA fiber and PE fiber, thus resulting in significant variations in the interface properties between the fiber and the matrix. PVA fiber has hydrophilic properties; hence, the free water in the specimens might have been reduced, thus potentially leading to a decrease in the dynamic compressive strength enhancement at high strain rates. The test results indicated that, at strain rates of 50 s^{-1} to 100 s^{-1} , the dynamic compressive strength of the PVA–EGC with a volume fraction of 0.5% of PVA fibers decreased instead of increasing compared to the matrix without fibers. This study systematically examined how varying the PE fiber content influenced the dynamic compressive behavior of the PE–EGC across different strain rates, thus utilizing the SHPB experimental setup and contributing to a deeper understanding of the reinforcing effects of PVA fiber and PE fiber, which are two commonly used fibers in EGCs. Additionally, the workability, quasistatic compressive, and quasistatic tensile properties were assessed. By integrating the empirical data, a modified CEB-FIP model, accounting for fiber content, was introduced, thus yielding favorable fitting outcomes. These findings were anticipated to enhance the comprehension of the PE–EGC's dynamic mechanical characteristics and have offered backing for its real-world utilization in high strain rate conditions. Figure 1 shows the flow chart of this study.

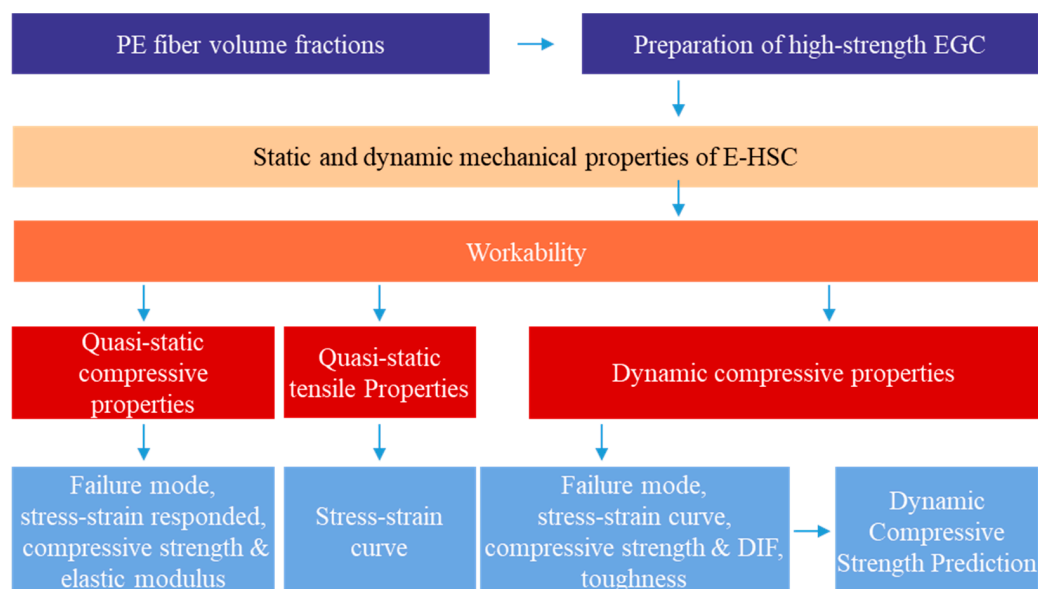


Figure 1. Flow chart.

2. Materials and Methods

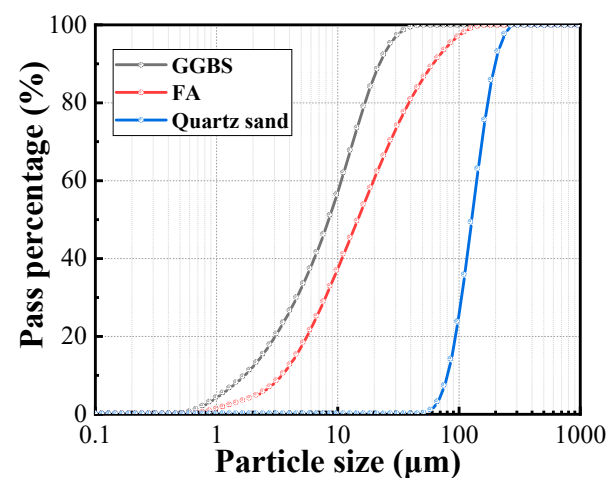
2.1. Materials

In this study, EGC was composed of FA, GGBS, alkali activator, quartz sand, retarder, water, and fiber. FA and GGBS, processed by Henan Hougang Co., Ltd., Zhengzhou, China, were used in accordance with the Chinese standard GB/T 18046-2017 [42], and their chemical compositions are presented in Table 1. The particle size distributions of the precursors and quartz sand are shown in Figure 2. The activator solution was prepared by mixing 10 M SH, processed by XiLONG SCIENTIFIC Co., Ltd., Guangzhou, China, with SS solution from Jiashan County Yourui Refractory Materials Co., Ltd., Jiaxing, China, thus achieving a modulus of 2.3. Quartz sand was used as the fine aggregate, with an average particle size of approximately $100 \mu\text{m}$ and a D_{50} of $126 \mu\text{m}$. BaCl_2 was used as a retarder to prolong the setting time of the fresh matrix. BaCl_2 not only delayed the hydration of GGBS, thereby prolonging the setting time, but also enhanced workability [43]. The physical parameters of the PE fiber are listed in Table 2.

Table 1. Chemical composition of FA and GGBS.

Composition	wt %	
	GGBS	FA
CaO	34.00	4.01
SiO ₂	34.50	54.00
Al ₂ O ₃	17.70	31.20
SO ₃	1.64	2.20
Fe ₂ O ₃	1.03	4.16
MgO	6.01	1.01
TiO ₂	/	1.13
Other	5.12	2.37
LOI (%)	0.84	4.60

LOI = loss on ignition.

**Figure 2.** Particle size distributions of the components.**Table 2.** Physical and mechanical properties of PE fiber.

Diameter (μm)	Length (mm)	Young's Modulus (GPa)	Elongation (%)	Strength (MPa)	Density (g/cm ³)
24	12	116	1–3	3000	0.97

2.2. Mix Proportions

To explore the influence of fiber volume fraction on EGC's quasistatic and dynamic behavior, five mixtures were employed. Based on previous research [32], a FA/GGBS ratio of 0.7:0.3 was adopted. As indicated earlier, including a certain proportion of slag can enhance the early strength of the mixture. These mixtures comprised a reference mixture (M) devoid of fiber and four additional mixtures with varying fiber volume fractions (based on concrete volume). Detailed mix proportions for all five mixtures, including the SS/SH ratio of 2.0 and the sand-to-binder ratio of 0.16, are presented in Table 3.

Table 3. Mix properties of EGC (kg/m³).

Mix IDs.	Binder		Quartz Sand	Activator		Water	BaCl ₂	PE Fiber (%vol.)	$V_f L_f/d_f$
	FA	GGBS		SH	SS				
M								0.0	0
PE0.5								0.5	2.5
PE1.0	849.7	364.1	242.8	161.8	323.7	72.8	12.1	1.0	5.0
PE1.5								1.5	7.5
PE2.0								2.0	10.0

Where V_f , L_f , and d_f represent fiber volume, length, and diameter, respectively.

2.3. Specimen Preparation

The mixing process is illustrated in Figure 3. Dry ingredients (FA, GGBS, sand, and retarder) were mixed for 2 min at the beginning of the mixing process. Following the dry mixing, the premixed and cooled activator solution was incorporated into the mixture. The combined materials were stirred for 3 min at 75 rpm to achieve a homogenous and flowable geopolymer matrix. PE fiber was then uniformly added and mixed for 3 min. This was followed by an additional 3 min of mixing to achieve a uniform and homogenous EGC. The freshly mixed EGC was promptly cast into molds and vibrated on a vibrating table for 2 min to eliminate entrapped air bubbles. To prevent the formation of shrinkage cracks and slow down moisture loss, all specimens were sealed with plastic film upon casting and remained indoors for 24 h. After demolding, the specimens underwent water curing for 27 days.

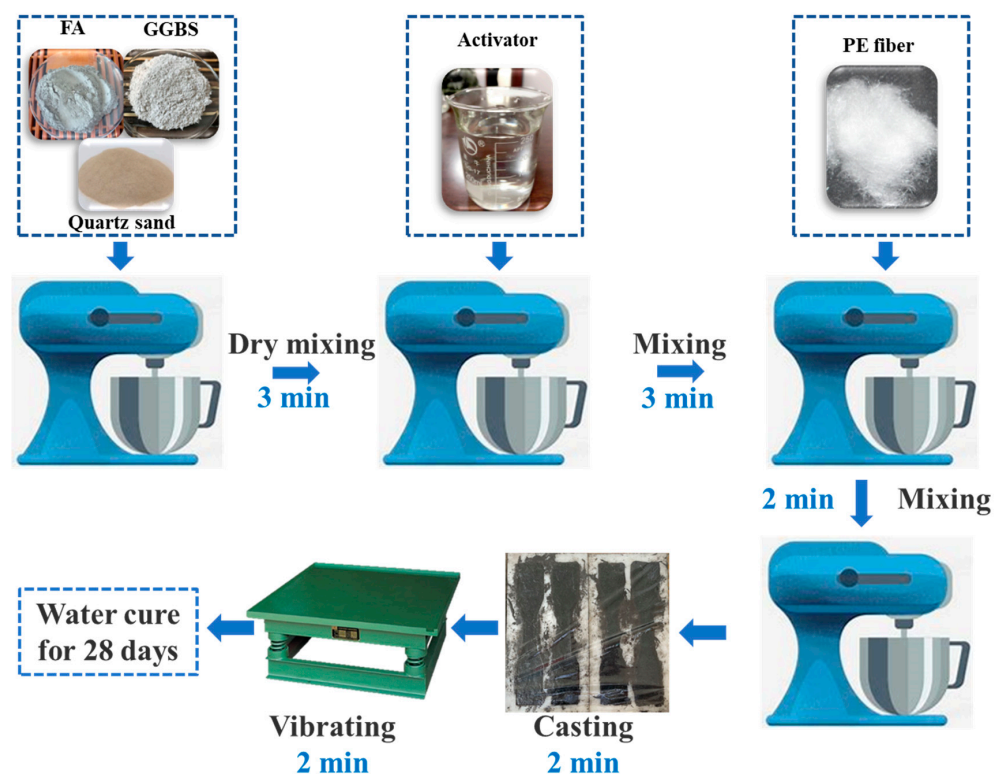


Figure 3. The mixing process.

2.4. Tests and Instrumentation

2.4.1. Flowability Test

Flowability tests were performed on all mixtures in accordance with ASTM-C1437-13 [44]. The fresh EGC was cast into a conical mold in two layers, with each layer being thoroughly compacted with a tamping rod. After lifting the mold vertically, the fresh mixture was subjected to 25 jolts. The two diameters of the fresh mixture in the vertical direction were measured, and their average value was reported.

2.4.2. Quasistatic Test

To evaluate the tensile strain-hardening behavior of EGC, tensile tests were performed, as illustrated in Figure 4. The tensile specimens were dumbbell-shaped with dimensions of 330 mm × 60 mm × 13 mm. Each mixture was subjected to tensile test with six samples. Representative stress–strain curves were presented. Tensile tests were performed according to JSCE-2008 [45] using a displacement-controlled mode with a speed of 0.5 mm/min. Two linear variable displacement transducers (LVDTs) were employed on opposite sides of the specimen's center to measure tensile deformation during the test.

2.4.3. Axial Impact Test

The Split Hopkinson Pressure Bar (SHPB) test is widely employed experimental methodology for understanding the mechanical response of materials subjected to high strain rate loading conditions, as illustrated in Figure 6. The data analysis system processed the collected signals into waveforms used to calculate the stress and strain experienced by the cylindrical specimens (100 mm diameter and 50 mm height). Additionally, one-dimensional stress waves generated by the projectile impact on the incident rod are susceptible to environmental factors and the material properties of the SHPB rods. This susceptibility can introduce unstable oscillations in the data. Therefore, to meet the assumption of uniform stress distribution and reduce high-frequency stress waves while extending the rise time of the incident wave, copper disks measuring 20 mm in diameter and 2 mm in thickness were chosen as waveform shapers.

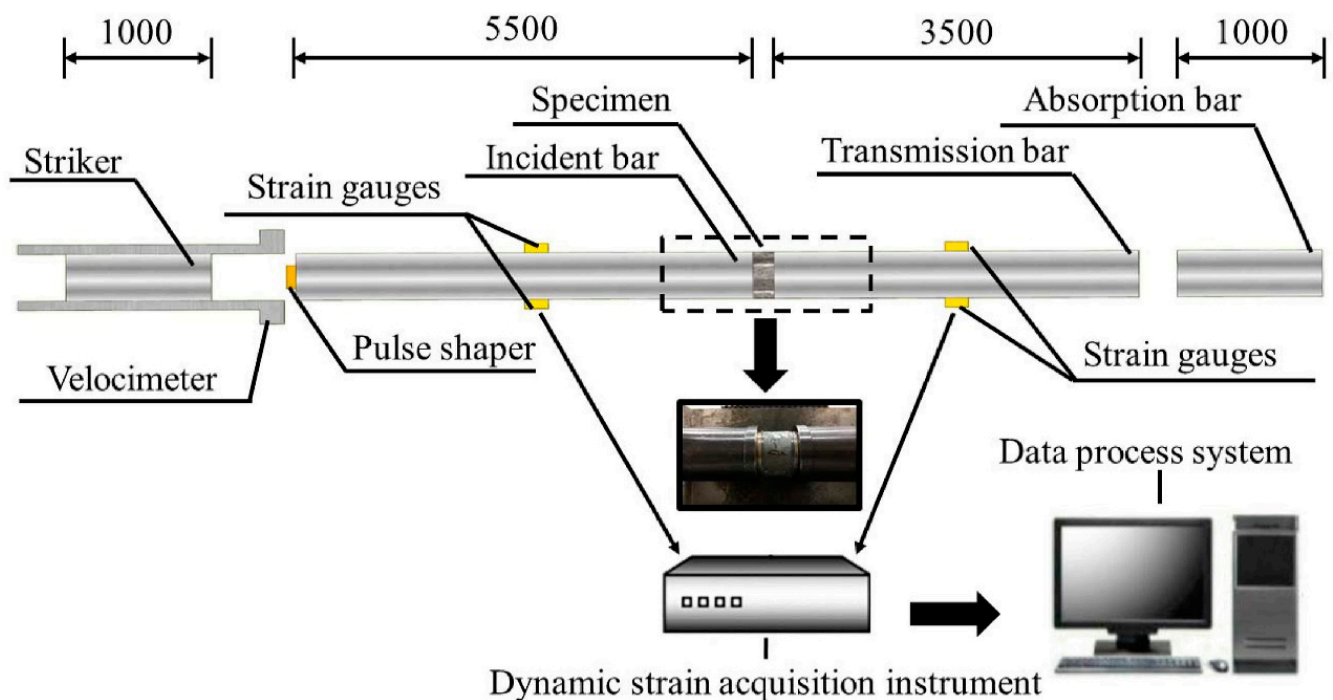


Figure 6. Schematic diagram of split Hopkinson pressure bar (unit: mm) [48].

According to the principles of one-dimensional stress waves [49] and based on the assumption of stress uniformity, the average stress $\sigma(t)$, strain $\epsilon(t)$, and strain rate $\dot{\epsilon}(t)$ of the specimen can be determined by Equation (1).

$$\begin{cases} \sigma(t) = \frac{A_b E_b}{A_0} \epsilon_t(t) \\ \dot{\epsilon}(t) = \frac{-2C_b}{l_0} \epsilon_r(t) \\ \epsilon(t) = \frac{-2C_b}{l_0} \int \epsilon_r(t) dt \end{cases} \quad (1)$$

where E_b , A_b and C_b represent the elastic modulus (MPa), cross-sectional area (mm^2), and longitudinal wave velocity (m/s) of the bar, respectively. A_0 and l_0 represent the cross-sectional area (mm^2) and thickness (mm) of the test specimen, respectively. Sample tests confirmed stress equilibrium, thus fulfilling the uniformity assumption (Figure 7).

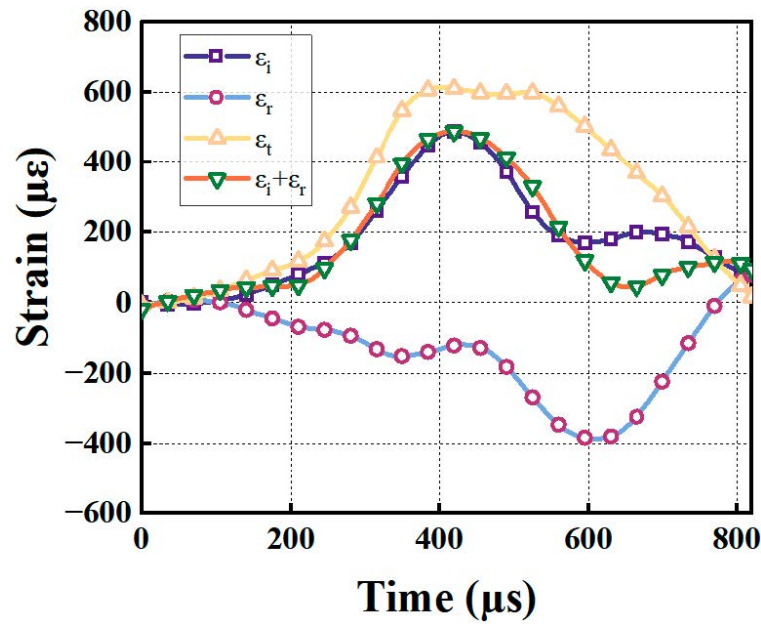


Figure 7. Waveform after aligning starting points.

3. Results and Discussion

3.1. Flowability

The results of the flowability tests conducted on all mixtures are depicted in Figure 8, thereby illustrating a gradual decrease in the slump flow of the fresh geopolymer pastes as the PE fiber content increased. The slump flow of the mixtures was significantly impacted by the PE fiber content. When the PE fiber content was low, the distance between the fiber in the paste was relatively large, thus making it difficult for the fiber to overlap and aggregate. However, with an increase in the PE fiber content, the likelihood of fiber overlap and aggregation between the fiber increased, thereby leading to increased internal flow resistance caused by fiber bridging [50]. Furthermore, related studies [51] have indicated that the mixing process promotes the formation of a water film around the PE fiber, thus reducing the available lubrication water and contributing to the observed decrease in the slump flow of the geopolymer paste.

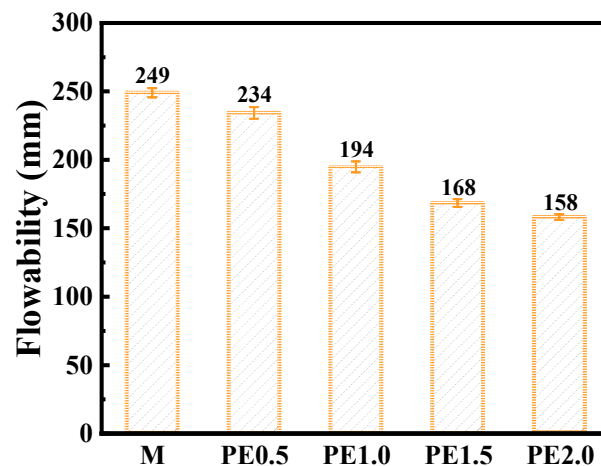


Figure 8. Effect of fiber length on flowability.

3.2. Quasistatic Compressive Properties

Figure 9 illustrates the failure modes of the EGC with varying PE fiber content. It is evident from Figure 9 that the failure mode of the geopolymer matrix without fiber

(Group M) significantly differed from that of the other groups. During the continuous compressive process at both ends of the specimen, the strain energy accumulated internally. When microcracks appeared, the internal energy was instantly released, thus leading to multiple block fractures in Group M specimens [52]. Upon the addition of fiber, due to their bridging effect, the specimen did not fracture immediately upon reaching the ultimate compressive strength. Instead, it swiftly formed a longitudinally penetrating oblique crack. After loading, there was no observable spalling of fragments on the specimen surface, thereby maintaining its excellent integrity. While adding PE fiber enhanced the postfailure integrity of the specimens, it did not change their brittle fracture behavior. No significant changes in the failure mode of the specimens were observed with increasing fiber content.

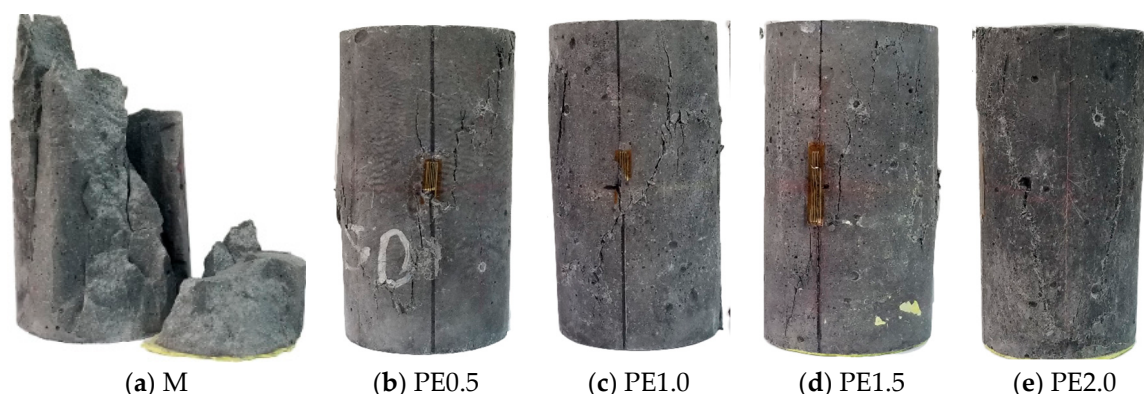


Figure 9. Quasistatic representative compressive failure modes of all mixtures.

The stress–strain response of all the mixtures after quasistatic testing is shown in Figure 10. It can be observed from Figure 10 that all mixtures exhibited brittle failure. Due to the specimens' brittle failure, data from the descending portion of the curves were unavailable. In the initial loading stage of the specimens, the stress and strain changed proportionally, thus approaching a straight line indicating the predominant role of the geopolymer matrix at this stage. After reaching the ultimate axial compressive strength, the stress of the Group M specimens sharply dropped, thereby indicating the loss of load-bearing capacity. Upon the addition of PE fiber, the stress also sharply declined after reaching the peak value. As the fiber content increased further, the bridging effect of the fiber strengthened, thus resulting in some residual strength in the specimens.

As shown in Figure 11, the PE fiber content influenced the compressive strength and elastic modulus of the EGC subjected to static axial compressive loading. The static compressive strength of the reference mixture (Group M) was 109 MPa. The compressive strength of the specimens showed a significant decrease as the PE fiber content increased. Compared to the reference mixture, PE2.0 displayed a 22% decrease in compressive strength. Overall, the compressive strength of the EGC decreased as the fiber content increased, which is consistent with previous research [53]. A similar decreasing trend was observed in the elastic modulus as in the compressive strength. Compared to the reference mixture, the elastic modulus of all the fiber-containing mixtures decreased by 15.0% to 28.5%. The decrease in both the compressive strength and elastic modulus was likely due to the impact of fiber on the mixture's flowability. This led to fiber overlap and aggregation, which reduced the density of the geopolymer matrix [8]. Consequently, the overall compressive strength and elastic modulus of the geopolymer material decreased [54]. Moreover, due to the hydrophobic nature of the PE fiber and its differing bonding properties with the matrix, it may not have effectively enhanced compressive strength. Therefore, a decrease in the compressive strength of the EGC relative to the M matrix was observed, thus ranging from 20.1% to 25.5%.

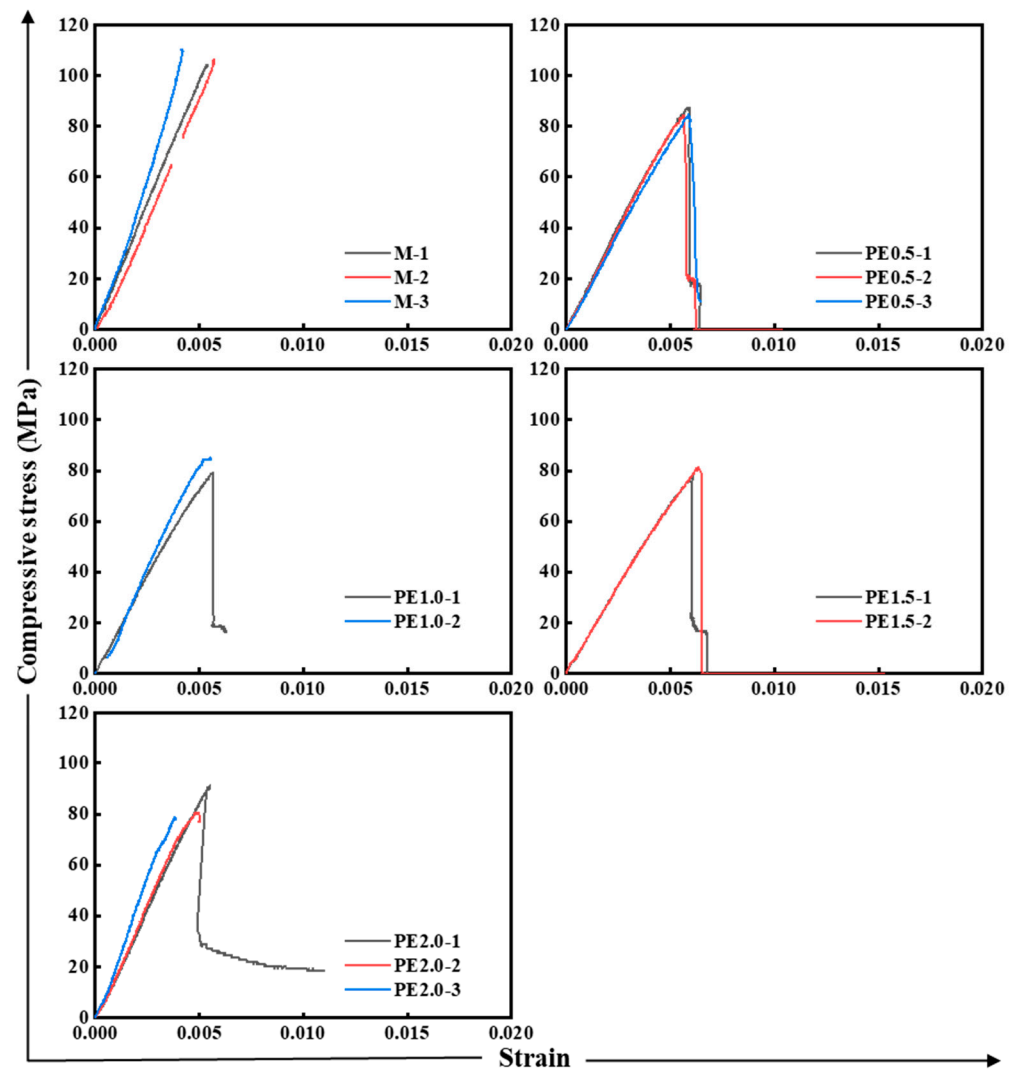


Figure 10. Stress–strain curves of quasistatic compressive tests.

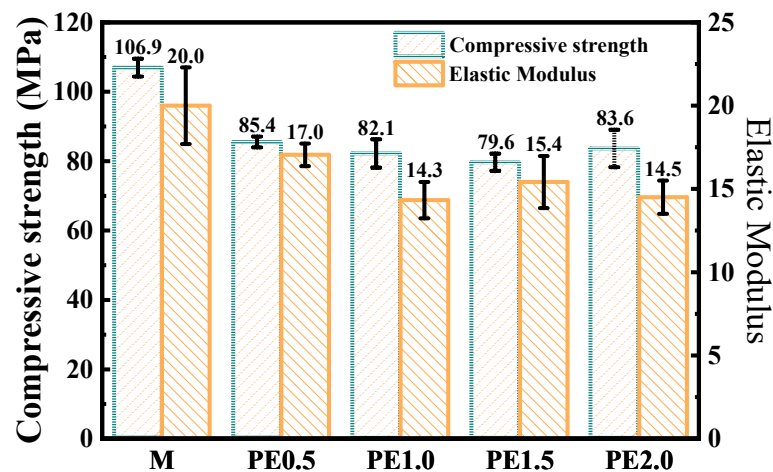


Figure 11. Quasistatic compressive strength of cylinder for all mixtures.

3.3. Quasistatic Tensile Properties

Figure 12b illustrates the typical tensile failure modes of the EGC with fiber contents ranging from 0.5% to 2.0%. The reference concrete displayed a failure mode characterized by single crack propagation, thus indicating brittle fracture characteristics. Thus, the dis-

cussion primarily centered on the failure modes observed in the EGC specimens containing fiber. Since not every crack traversed the entire specimen in its entirety, some of the cracks may be present in only a portion of the width of the specimen. Therefore, in this study, in order to have a more accurate count of the number of cracks in the specimen, the number of cracks that crossed the four equidistant lines in the transverse direction of the specimen were counted and averaged to obtain the number of cracks in each specimen, as shown in Figure 12a. In addition, in order to avoid the interference of the displacement gauge fixture on the crack observation, this study reported the number and width of cracks in the 60 mm observation section in the middle of the specimen. Finally, the average number of cracks for three specimens of each mixture was reported. The crack widths were calculated based on the number of cracks, as well as the deformation of the scale length, at which time it was assumed that the matrix deformation was negligible [22]. From Figure 12b and Table 4, it can be observed that the number of cracks in the specimens gradually increased, which is consistent with the trend of fiber content variation. PE 2.0 exhibited the greatest tensile strain capacity among all the mixtures and also had the greatest number of cracks. The average crack number increased by 314.0% and 96.6% when the fiber content increased from 0.5% to 1.0% and 1.5%, respectively, but it only increased by 12.9% when the fiber content increased from 1.5% to 2.0%. From this, it can be inferred that the ability of further increasing the fiber content from 1.5% to induce cracks decreases significantly. There was a gradual decrease in the average crack width as the fiber content increased from 0.5% to 1.0% and 1.5%. Compared to PE1.5, the average crack width in PE2.0 increased by 4.1 μm , but it only increased by 2.7%. Overall, as the fiber content increased, the number of fibers at both ends of the crack increased, and so did the fiber bridging capacity [53].

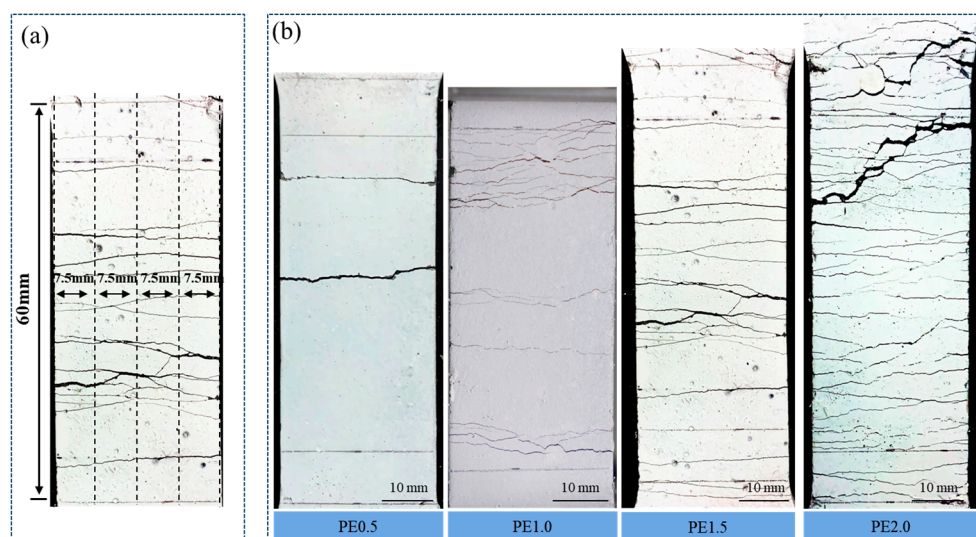


Figure 12. Schematic diagram of statistical method of crack number and typical tensile failure modes of EGC: (a) statistical method; (b) typical tensile failure modes.

Table 4. Average crack number and average crack width of EGC.

Mix IDs	Average Crack Number	Average Crack Width (μm)
PE0.5	2 (1)	246.9 (43.9)
PE1.0	15 (3)	173.0 (54.1)
PE1.5	19 (5)	148.4 (27.9)
PE2.0	21 (4)	152.5 (18.3)

Data in parentheses are standard deviations.

The stress–strain curves for all mixtures are depicted in Figure 13. All EGC samples, except for the reference mixture M, exhibited strain-hardening behavior under tensile loading. In contrast to its compressive behavior, the tensile properties of the EGC, including

tensile strength and ultimate strain, gradually improved with increasing fiber content. PE1.0 exhibited a tensile strength of 2.90 MPa and an ultimate strain of 4.26%. A significant strain-hardening stage was observed during which cracks continuously initiated and propagated, thus leading to noticeable fluctuations in the stress–strain curve. When the fiber content increased to 1.5%, the tensile strength of PE1.5 reached 5.63 MPa, with an ultimate strain of 4.70%. This represents an increase of 94.1% and 10.3%, respectively, compared to PE1.0. Additionally, the tensile strength and ultimate strain of PE2.0 were 10.1% and 16.0% higher, respectively, than those of PE1.5. As the number of cracks increased, the stress–strain curve also exhibited more fluctuations. As the fiber volume fraction increased, the fiber reinforcement index ($V_f L_f/d_f$) of PE0.5, PE1.0, PE1.5, and PE2.0 increased from 2.50 to 5.00, 7.50, and 10.0, respectively, thus significantly enhancing the tensile performance of the EGC. Due to the inherent hydrophobicity of the PE fiber, the interface adhesion between the fiber and the matrix was mainly achieved through friction. As the fiber content increased, this mechanism facilitated an increase in the number of fiber bridging cracks, thereby ultimately resulting in the enhancement of the tensile strength of the EGC [53].

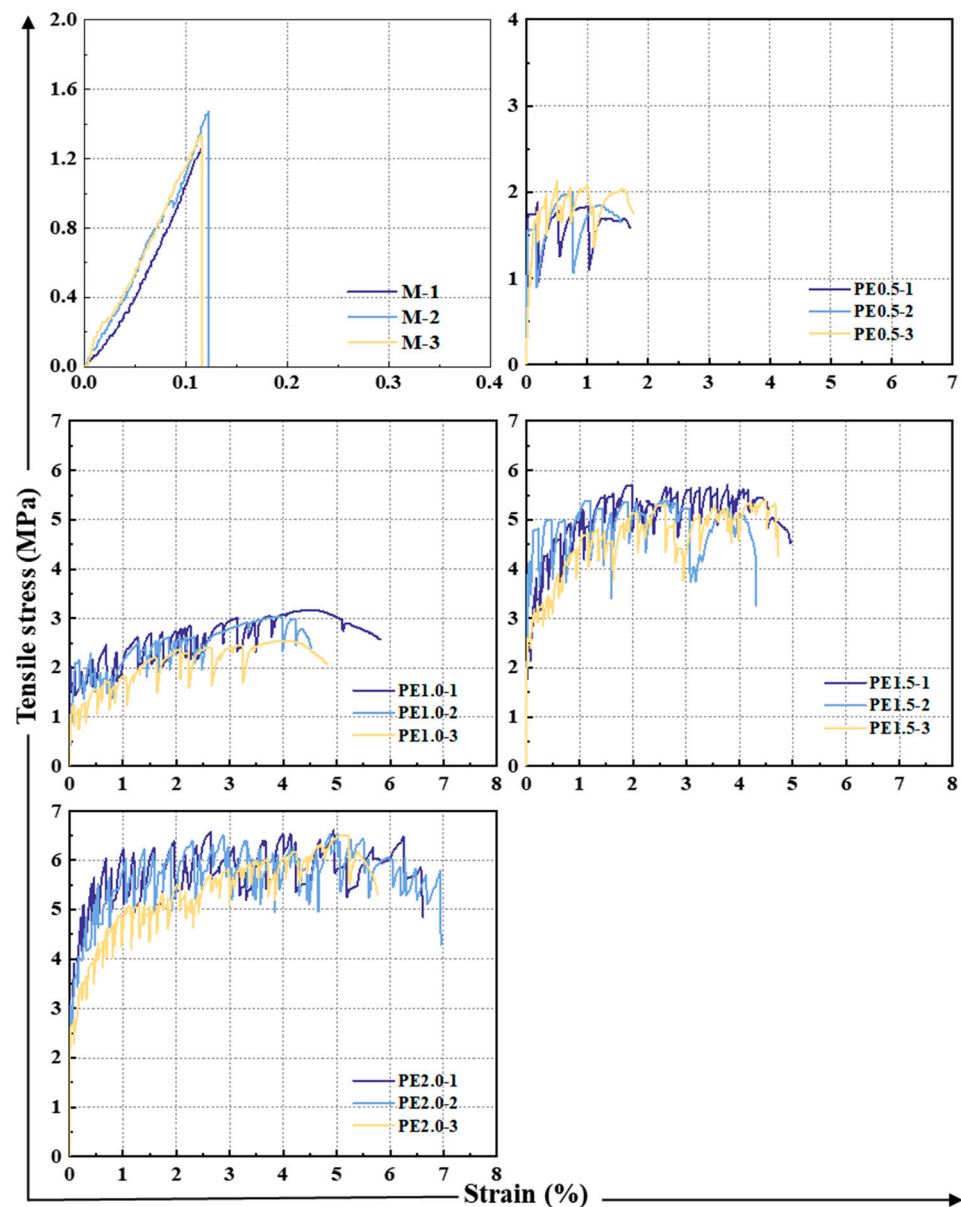


Figure 13. Quasistatic uniaxial tensile stress–strain curves of all mixtures.

3.4. Dynamic Compressive Properties of EGC

3.4.1. Failure Mode

Figure 14 depicts the failure modes of the specimens under impact loading at varying strain rates. The observed trend indicates an intensification of fragmentation with increasing strain rate. This was characterized by a rise in the number of smaller fragments with reduced volume, alongside a significant increase in both the number and width of cracks. The reference specimens, without fiber, exhibited a pulverized failure mode under various strain rates. The inclusion of the PE fiber demonstrably restrained the lateral deformation experienced by the specimens, thereby inducing a notable alteration in their failure mode. Observation of the fracture surfaces revealed numerous fibers bridging various small fragments. Figure 14 reveals a continuous improvement in the integrity of the EGC specimens at all strain rates with increasing fiber volume. This enhancement was attributed to the bridging effect of the fiber. Similar phenomena have been observed in studies on concrete reinforced with steel fibers and organic fibers [48,55]. At a strain rate of approximately 120 s^{-1} , increasing the volume fraction of the PE fiber resulted in a decrease in both the number of fragments and crack widths. This phenomenon was attributed to the enhanced bridging effect of the fiber, which hindered crack propagation and facilitated energy dissipation. However, exceeding a strain rate of 155 s^{-1} compromised the integrity of the EGC specimens.



Figure 14. Failure patterns of all mixtures under impact loadings: (a) M, (b) PE0.5, (c) PE1.0, (c) PE1.0, (d) PE1.5, (e) PE2.0.

3.4.2. Stress–Strain Relationship

Figure 15 depicts the stress–strain curves for the matrix and the EGC at different strain rates. Determining a constant strain rate has been a major challenge in SHPB experiments, so choosing an accurate strain rate measurement method is critical. For this experiment, the strain rate was chosen based on the slope of the main linear portion identified in the strain–time curve during the uniform deformation phase of specimen loading. Figure 15 depicts all the groups exhibiting a pronounced linear relationship in their stress–strain curves before the peak stress. This indicates a clear elastic stage, with stress directly proportional to strain. Subsequently, the curve enters a nonlinear strengthening stage, during which cracks initiate and propagate, and fiber bridges to restrain crack propagation [38,56]. A notable difference was observed between the descending portions of the dynamic and static stress–strain curves. The descending segment of the static curve was characterized by a pronounced decline, whereas the descending segment of the dynamic curve exhibited gradual and relatively flat behavior. During this stage, cracks rapidly developed, thus leading to the formation of large cracks and eventual fracture. Throughout the process from crack initiation to specimen failure, most fibers experienced processes such as debonding, pull-out, or fracture from the matrix, thus consuming a considerable amount of energy [57]. With increasing strain rates, an increase in the strain rate resulted in a steeper slope for the linear portion of the curve.

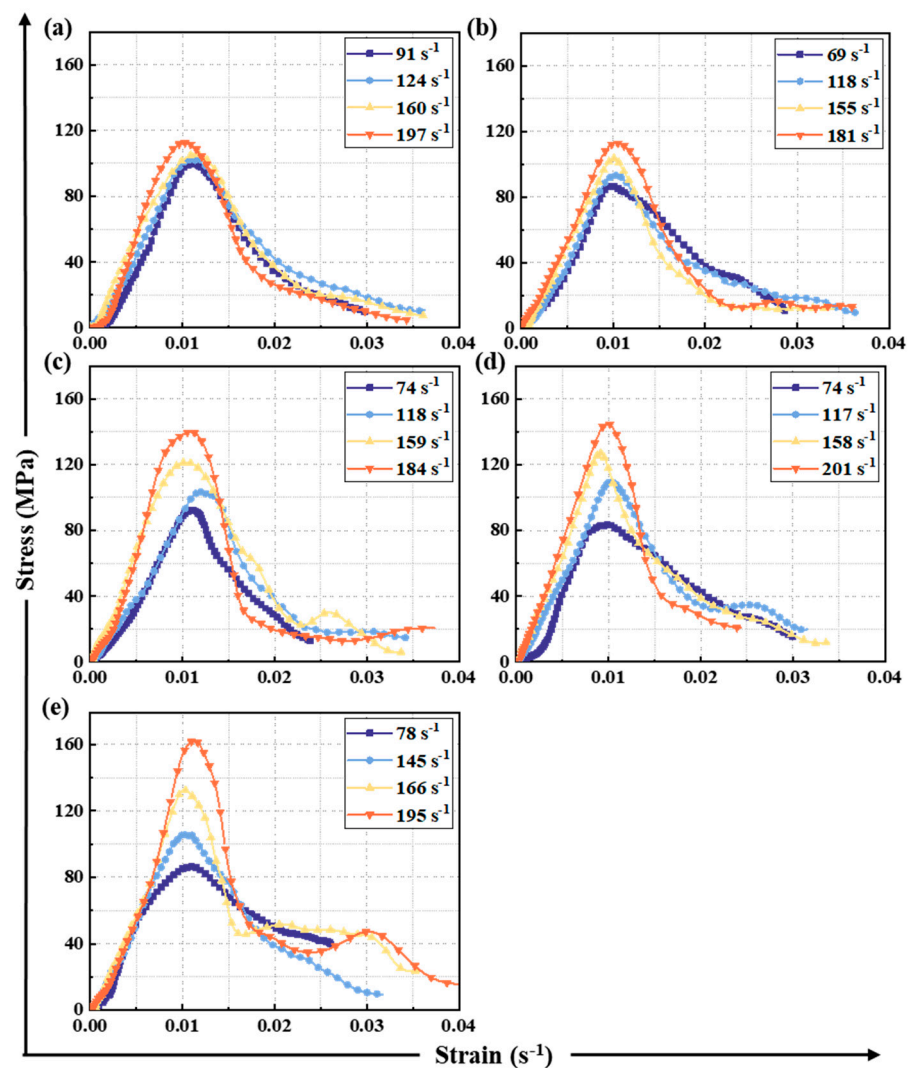


Figure 15. Dynamic compressive stress–strain curves under different strain rates: (a) M, (b) PE0.5, (c) PE1.0, (d) PE1.5, (e) PE2.0.

3.4.3. Dynamic Strength and Dynamic Increase Factor

The dynamic compressive strength of all the mixtures across different strain rates is presented in Figure 16. An increase in the strain rate was accompanied by a gradual increase in the dynamic compressive strength of the specimens, thus suggesting a degree of linearity in their response. This observation highlights the sensitivity of the specimens to strain rate. Two main factors may contribute to this phenomenon: First, in dynamic compressive tests, the short loading time of the specimens prevented microcracks from maturing into macrocracks. To dissipate the transferred energy, a large number of microcracks needed to form within a short period, which consumed more energy. A direct correlation was observed between the increase in the strain rate and the corresponding rise in the number of cracks, thus leading to the enhancement of the dynamic ultimate compressive strength. Secondly, during high-speed impact processes, the inertia effect of the peripheral parts of the specimens inhibited the lateral deformation of the central part, thus resulting in the specimens being in a confined state. Higher strain rates enhanced the inhibitory effect, thus resulting in increased dynamic ultimate compressive strength.

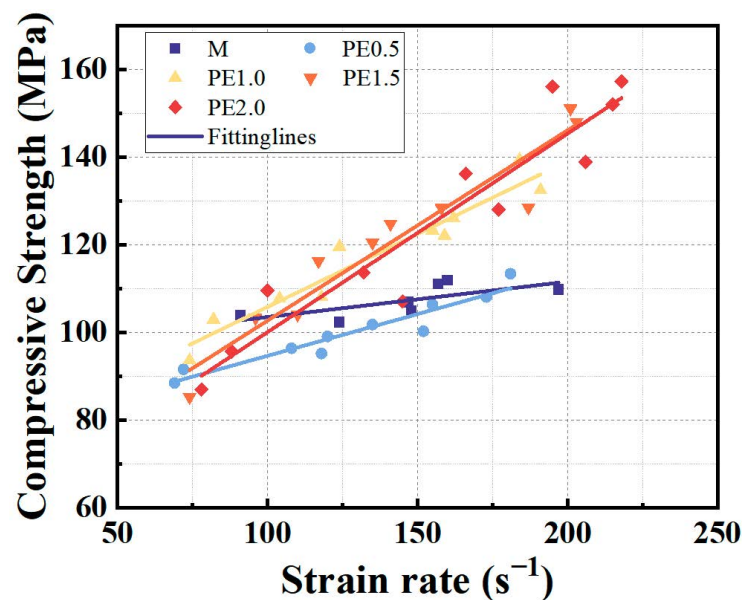


Figure 16. Dynamic compressive strength strain of all mixture versus strain rate.

The influence of the PE fiber content and strain rate on the dynamic compressive strength was evident. Specimens without fiber exhibited a moderate strength increase (18.1%) from 94.8 MPa to 112 MPa, as the strain rate rose from 73.0 s⁻¹ to 160 s⁻¹. However, the presence of PE fiber significantly enhanced this trend. At fiber volume fractions of 0.5% and 2%, the strength increased by 28.1% and 79.4%, respectively, with increasing strain rate. This indicates a stronger reinforcing effect with higher fiber content. It is worth noting that at low strain rates, the fiber-free specimens displayed slightly higher strength. However, this trend reversed at higher strain rates, with fiber-reinforced specimens exceeding or matching those without fibers. However, when the content of PE fibers was higher, the fibers tended to agglomerate more easily, thereby leading to uneven distribution within the specimens and an increase in internal defects [58]. Therefore, overall, the dynamic ultimate compressive strength of the specimens with 2% fiber content, represented by PE2.0, was slightly lower than that of the specimens with 1.5% fiber content, represented by PE1.5.

3.4.4. Dynamic Increase Factor

The dynamic increase factor (DIF) has been widely used to assess the strain rate sensitivity of dynamic compressive strength. Multiple studies have reported a log-linear relationship between the dynamic compressive strength of concrete-like materials and the strain rate using a base 10 logarithm. In this investigation, Equation (2) was utilized to

describe the relationship observed between the EGC and the strain rate. The findings are presented visually in Figure 15.

$$\text{DIF} = a \lg \dot{\epsilon} + b \quad (2)$$

where represents the strain rate. Table 5 presents the results of parameters a and b for different groups.

Table 5. Values of parameters a and b in different EGC specimens.

Mix IDs	a	b
M	0.232	0.503
PE0.5	0.570	−0.023
PE1.0	1.16	−1.01
PE1.5	1.72	−2.12
PE2.0	1.71	−2.20

As shown in Figure 17, the DIF of the specimens exhibited a strain rate-dependent increase. Worthy of note was the significant increase in the strain rate sensitivity of the geopolymer concrete observed upon the addition of fiber, irrespective of the fiber content. In comparison to the reference mixture, the slope of the DIF for PE0.5 increased from 0.232 to 0.570, while for PE1.0, the slope increased to 1.16, thus emphasizing once again the important role of fiber in strain rate sensitivity. When explaining the reasons for the strain rate sensitivity, the lateral inertial effect was widely considered as a significant factor [59–61]. The addition of PE fiber provided additional resistance to concrete crack propagation, thus increasing the strain rate sensitivity. Similar phenomena have also been observed in geopolymer concrete reinforced with PVA fiber, where the presence of PVA fiber increased the DIF by more than 3.56 times compared to ordinary geopolymer concrete [33,38,55].

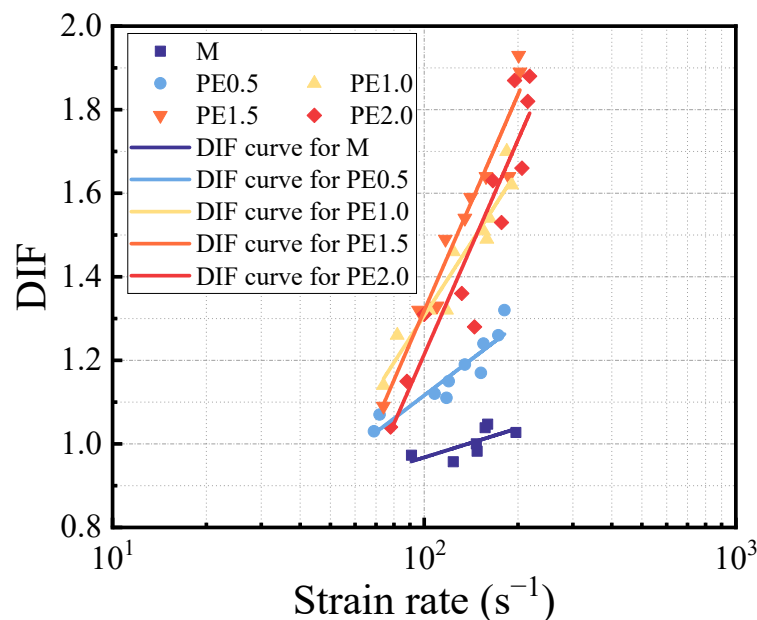


Figure 17. Summary of fitted logarithm curves for all mixtures.

3.4.5. Dynamic Toughness

Dynamic toughness, the ability of a material to absorb energy, is quantified by the area under the stress–strain curve and reflects its resistance to impact. The impact toughness of a material can be calculated by using Equation (3), which computes the area enclosed by the stress–strain curve.

$$W = \int_0^{\epsilon} \sigma(\epsilon) d\epsilon \quad (3)$$

Figure 18 illustrates the impact of the PE fiber volume fraction on the dynamic impact toughness under various strain rates. An overall increase in the specimens' impact toughness to impact was observed with an increasing strain rate. Figure 16 shows that the impact toughness of the specimens generally increased with the increase in the strain rate. For example, when the strain rate was increased from 74 s^{-1} to 158 s^{-1} and 201 s^{-1} , the impact toughness of PE1.5 increased by 40.0% and 54.6%, respectively. This observation indicated the strain rate sensitivity of both the reference concrete and the EGC. Across all strain rates, specimens containing PE fiber exhibited higher dynamic impact toughness compared to the reference concrete. It was further observed that the impact toughness of PE0.5 displayed a close resemblance to that of the reference concrete, while the impact toughness of PE1.0 demonstrated a similar level of toughness to PE1.5. This was attributed to the bridging of cracks by the PE fiber during crack propagation, thus leading to debonding, sliding, or pull-out behavior, as well as increasing the energy absorption capacity and enhancing the specimen's impact toughness. Moreover, considering the diameter of the PE fiber, even with only a 1% volume fraction, there was still enough fiber present in the concrete to form a grid [62]. Hence, there was little difference in the impact toughness between PE1.0 and PE1.5. At low strain rates ($<90 \text{ s}^{-1}$), the specimens with PE fiber ranging from 0.5% to 1.5% in volume exhibited similar dynamic impact toughness values. The application of higher strain rates resulted in more extensive damage to the specimens, which was characterized by an increased number and size of cracks, elevated peak strain values, and a marked improvement in the energy absorption capacity exhibited by the fiber [63]. Therefore, under highly damaged conditions, the fiber with higher volume fractions could absorb more energy, with PE2.0 exhibiting the maximum impact toughness. Additionally, PE2.0 demonstrated the highest compressive strength exhibited under high strain rate loading conditions, which also contributed to its maximum impact toughness.

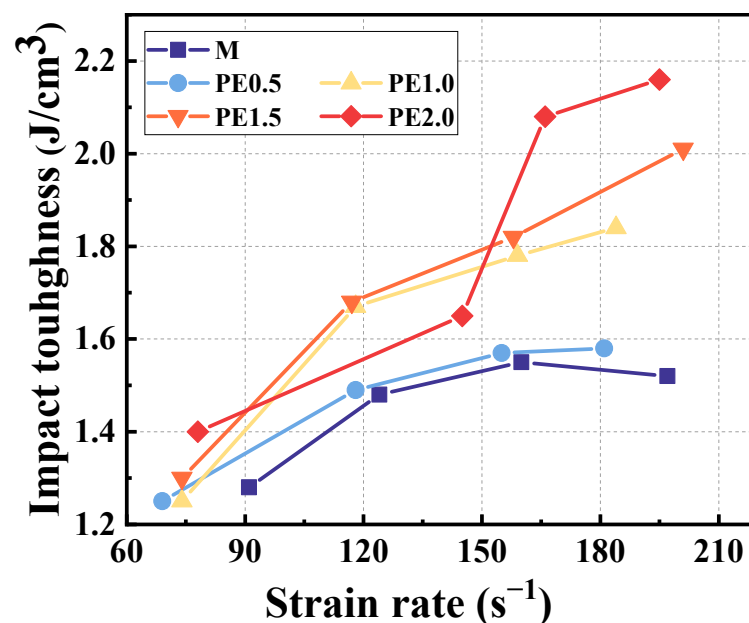


Figure 18. The impact toughness of geopolymer mixtures under different strain rate.

3.4.6. Dynamic Compressive Strength Prediction

In the past, several typical DIF prediction formulas have been developed concerning the relationship between the DIF and strain rate. These formulas can be broadly categorized into two types: those based on power law variations and those adopting logarithmic functions. A review of typical DIF prediction formulas has been provided here. Among these,

the CEB-FIP model, developed by the Comité Euro-International du Béton, has received particular attention due to its widespread adoption [64]. The expression is provided below:

$$\text{DIF}_{\text{CEB-FIP}} = \begin{cases} (\dot{\epsilon}_c / \dot{\epsilon}_{c0})^{1.026\alpha} & \text{for } \dot{\epsilon} \leq 30 \text{ s}^{-1} \\ \gamma_s (\dot{\epsilon}_c / \dot{\epsilon}_{c0})^{1/3} & \text{for } \dot{\epsilon} \geq 30 \text{ s}^{-1} \end{cases} \quad (4)$$

Grote et al. [65] developed a formula for predicting the DIF in SHPB tests of cement mortar by utilizing a logarithmic function.

$$\text{DIF}_{\text{Grote}} = \begin{cases} 0.0235 \log \dot{\epsilon}_c + 1.07 & \text{for } \dot{\epsilon}_c \leq 266 \text{ s}^{-1} \\ 0.882 (\log \dot{\epsilon}_c)^3 - 4.48 (\log \dot{\epsilon}_c)^2 + 7.22 (\log \dot{\epsilon}_c) - 2.64 & \text{for } \dot{\epsilon}_c > 28.29 \text{ s}^{-1} \end{cases} \quad (5)$$

Khan et al. [33] conducted extensive experimental research on fiber-reinforced geopolymer concrete and proposed an empirical formula using a logarithmic function:

$$\text{DIF}_{\text{Khan}} = \begin{cases} 0.0128 \ln \dot{\epsilon}_c + 1.1709 & \text{for } \dot{\epsilon}_c \leq 66 \text{ s}^{-1} \\ 0.540 \ln \dot{\epsilon}_c - 0.9233 & \text{for } \dot{\epsilon}_c \geq 66 \text{ s}^{-1} \end{cases} \quad (6)$$

where $\alpha = \frac{1}{5+9f_{c,\text{imp}}/f_{\text{cm}0}}$, $f_{c,\text{imp}}$ is the impact compressive strength, and $f_{\text{cm}0} = 10 \text{ MPa}$, $\log^{\gamma_s} = 6\alpha - 2$.

A comparison of the empirical formulas' predictions with the experimental data is shown in Figure 19. The results indicate that these empirical formulas poorly matched the experimental data and failed to adequately describe the dynamic DIF response of the EGC. The applicability range of the empirical formula proposed by Grote et al. [65] deviated from the strain rate range of the experimental results, despite the absence of coarse aggregates in the mixtures used in this study and the inclusion of fiber components. On the other hand, the logarithmic function-based DIF prediction model proposed by Khan et al. [33] provided a better prediction of the experimental results at a strain rate of around 200 s^{-1} in this study but still tended to overestimate the DIF overall. In the CEB-FIP model, 80 MPa was selected as the input parameter for static compressive strength. The CEB-FIP model underestimated the transition strain rate, but its overall trend matched the experimental results. Additionally, composite materials with organic fiber seemed to have higher transition strain rates, which is consistent with previous research findings [38,61]. The significant influence of the fiber content on the EGC's DIF necessitated the development of a modified model. This model aims to accurately represent EGC's dynamic response across varying strain rates, thereby providing a reliable foundation for engineering applications and numerical simulations.

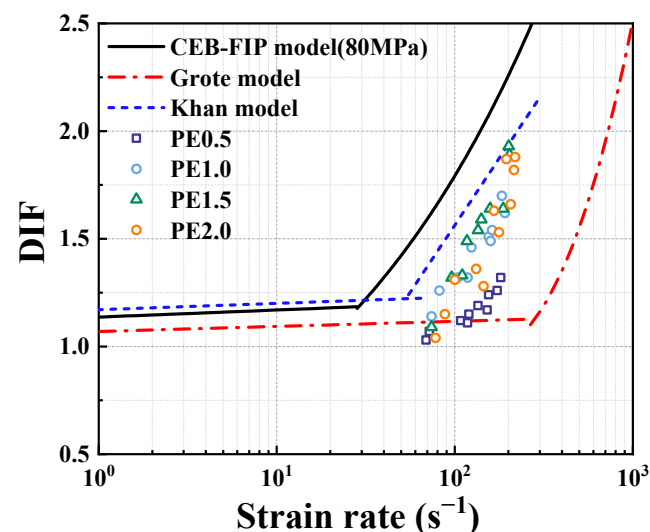


Figure 19. Comparison of DIF between the test results and existing models.

Drawing upon the experimental data, the strain rates were restricted to a range between 69 s^{-1} and 201 s^{-1} . Subsequently, a modified model, derived from the CEB-FIP model, was proposed to precisely predict the dynamic response of the EGC under dynamic loading. This model is expressed by Equation (7).

$$\text{DIF} = m\gamma_s \left(\frac{\dot{\epsilon}}{\dot{\epsilon}_c}\right)^{\frac{1}{3} \times n} \quad \text{for } 69 \text{ s}^{-1} \leq \dot{\epsilon} \leq 201 \text{ s}^{-1} \quad (7)$$

where $\dot{\epsilon}$ represents the loading strain rate, $\dot{\epsilon}_c = 0.00003 \text{ s}^{-1}$, and m and n are the parameters of considered account for the fiber content. The matching results between the modified model and the experimental data in this study are presented in Figure 20, with the outcomes of parameters m and n summarized in Table 6. As shown in Figure 20, the modified model exhibits good agreement with the experimental data. This highlights the effectiveness of the proposed modification in accurately capturing the dynamic response of the EGC across varying fiber contents. Furthermore, in order to validate the effectiveness of the proposed modified model, a comparison was conducted with previously obtained dynamic test results on PVA–EGC. The comparison results, as shown in Figure 21, demonstrate a good agreement [38]. However, it should be noted that this study did not precisely determine the transition strain rate of the EGC. In order to achieve a more comprehensive understanding of the dynamic behavior of the EGC, it is hoped that future studies will further explore and provide precise information regarding the transition strain rate of EGC. This deeper comprehension of the material’s mechanical properties under various strain rates will contribute to the development of more robust references for practical engineering applications.

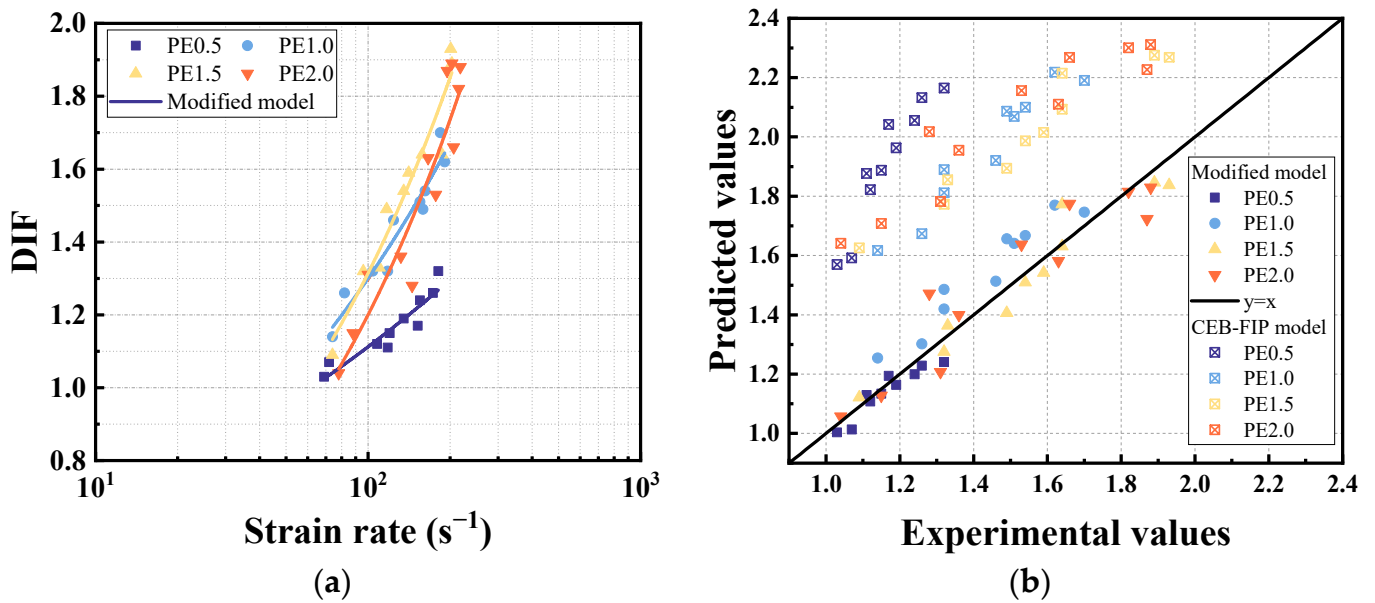


Figure 20. Verification of the proposed DIF model: (a) Modified model results of the DIF at different strain rate show good agreement with test results; (b) calculation versus experimental values.

Table 6. Parameters of DIF fitting equation.

Parameters	Fiber Volume Content			
	0.5%	1.0%	1.5%	2.0%
m	3.36	0.501	0.0648	0.0338
n	0.660	1.09	1.48	1.60

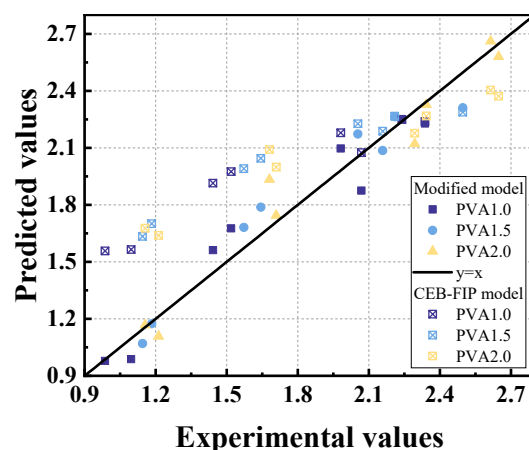


Figure 21. Modified model results of the DIF showed good agreement with test results [38].

4. Conclusions

This study investigated the influence of fiber content on various aspects of the EGC, including workability, quasistatic mechanical properties, and dynamic compressive performance. The following significant conclusions have been drawn from the experimental results:

- (1) The incorporation of PE fiber significantly enhanced the tensile properties of the EGC through fiber bridging, thus leading to significant strain-hardening behavior and improved compressive damage modes. However, with the increase in fiber content, the workability of the EGC decreased, thus leading to an increase in porosity and a decrease in compressive strength.
- (2) The EGC exhibited good impact resistance under high-rate impact loading, which was further enhanced with increasing fiber content. Under equivalent strain rates, the EGC maintained its integrity, while the reference concrete fractured into powder.
- (3) Compared to the reference concrete, the EGC showed higher strain rate sensitivity, with PE1.5 exhibiting the highest sensitivity. Increasing the strain rate led to a gradual improvement in the EGC's dynamic compressive performance, as evidenced by rising peak stress, dynamic increase factor, and impact toughness. Considering the workability, quasistatic mechanical properties, and dynamic compressive performance of the EGC, a 1.5% fiber volume content is optimal.
- (4) Considering the bridging effect of fiber, a modified model based on CEB-FIP was proposed and achieved a good fit, thus providing references for practical engineering applications and numerical models.

Compared to previous studies on the dynamic mechanical properties of PVA–EGC [36], this study found that PE fiber significantly increased the dynamic compressive strength of the EGC under dynamic loading. This indicates that PE fiber is more suitable for resisting various dynamic loading in EGC compared to PVA fiber. However, it was worth noting that although a modified model based on the CEB-FIP model was proposed in this study, the direct relationship between fiber content and parameters in the modified model has not been established. Further research is needed to provide a more comprehensive theoretical basis for engineering design.

Author Contributions: Conceptualization, Y.L.; methodology, Y.L.; formal analysis, X.Z. and W.Z.; investigation, X.Z. and W.Z.; resources, B.X.; data curation, B.X. and C.F.; writing—original draft preparation, Y.L. and X.Z.; writing—review and editing, B.X. and Y.L.; visualization, H.L. and J.Y.; project administration, B.X.; funding acquisition, B.X. All authors have read and agreed to the published version of the manuscript.

Funding: This research was funded by the Guangzhou Power Supply Bureau, Guangdong Power Grid Co., Ltd., China Southern Power Grid Co., Ltd., grant number 0301002023030103XG00073.

Data Availability Statement: The data presented in this study are available upon request from the corresponding author. The data are not publicly available due to confidentiality issues.

Conflicts of Interest: Yu Ling, Xiafei Zhang and Weiyu Zou were employed by the company Guangdong Power Grid Co., Ltd. and China Southern Power Grid Co., Ltd. The remaining authors declare that the research was conducted in the absence of any commercial or financial relationship that could be construed as a potential conflict of interest.

References

- Zhao, C.; Wang, Z.; Zhu, Z.; Guo, Q.; Wu, X.; Zhao, R. Research on different types of fiber reinforced concrete in recent years: An overview. *Constr. Build. Mater.* **2023**, *365*, 130075. [\[CrossRef\]](#)
- Wu, H.; Shen, A.; Ren, G.; Ma, Q.; Wang, Z.; Cheng, Q.; Li, Y. Dynamic mechanical properties of fiber-reinforced concrete: A review. *Constr. Build. Mater.* **2023**, *366*, 130145. [\[CrossRef\]](#)
- Chen, Z.; Pan, H.; Zhuo, K.; Su, J.; Xie, B.; Lin, J.; Guo, Y. Dynamic compressive behavior of environmentally friendly high-strength concrete: Experimental investigation and modelling. *Constr. Build. Mater.* **2024**, *427*, 136259. [\[CrossRef\]](#)
- Su, J.-Y.; Chen, G.; Pan, H.-S.; Lin, J.-X.; Zhang, J.; Zhuo, K.-X.; Chen, Z.-B.; Guo, Y.-C. Rubber modified high strength-high ductility concrete: Effect of rubber replacement ratio and fiber length. *Constr. Build. Mater.* **2023**, *404*, 133243. [\[CrossRef\]](#)
- Lin, J.-X.; Song, Y.; Xie, Z.-H.; Guo, Y.-C.; Yuan, B.; Zeng, J.-J.; Wei, X. Static and dynamic mechanical behavior of engineered cementitious composites with PP and PVA fibers. *J. Build. Eng.* **2020**, *29*, 101097. [\[CrossRef\]](#)
- Yu, K.; Li, L.; Yu, J.; Wang, Y.; Ye, J.; Xu, Q. Direct tensile properties of engineered cementitious composites: A review. *Constr. Build. Mater.* **2018**, *165*, 346–362. [\[CrossRef\]](#)
- Li, V.; Wu, C.; Wang, S.; Ogawa, A.; Saito, T. Interface Tailoring for Strain-hardening PVA-ECC. *ACI Mater. J.* **2011**, *99*, 463–472.
- Yu, K.; Ding, Y.; Liu, J.; Bai, Y. Energy dissipation characteristics of all-grade polyethylene fiber-reinforced engineered cementitious composites (PE-ECC). *Cem. Concr. Compos.* **2020**, *106*, 103459. [\[CrossRef\]](#)
- Singh, M.; Saini, B.; Chalak, H.D. Performance and composition analysis of engineered cementitious composite (ECC)—A review. *J. Build. Eng.* **2019**, *26*, 100851. [\[CrossRef\]](#)
- Chen, G.; Zheng, D.-P.; Chen, Y.-W.; Lin, J.-X.; Lao, W.-J.; Guo, Y.-C.; Chen, Z.-B.; Lan, X.-W. Development of high performance geopolymer concrete with waste rubber and recycle steel fiber: A study on compressive behavior, carbon emissions and economical performance. *Constr. Build. Mater.* **2023**, *393*, 131988. [\[CrossRef\]](#)
- Lee, W.K.W.; van Deventer, J.S.J. The interface between natural siliceous aggregates and geopolymers. *Cem. Concr. Res.* **2004**, *34*, 195–206. [\[CrossRef\]](#)
- Fernández-Jiménez, A.; Palomo, A.; Criado, M. Microstructure development of alkali-activated fly ash cement: A descriptive model. *Cem. Concr. Res.* **2005**, *35*, 1204–1209. [\[CrossRef\]](#)
- Al-mashhadani, M.M.; Canpolat, O.; Aygörmez, Y.; Uysal, M.; Erdem, S. Mechanical and microstructural characterization of fiber reinforced fly ash based geopolymer composites. *Constr. Build. Mater.* **2018**, *167*, 505–513. [\[CrossRef\]](#)
- Ranjbar, N.; Zhang, M. Fiber-reinforced geopolymer composites: A review. *Cem. Concr. Compos.* **2020**, *107*, 103498. [\[CrossRef\]](#)
- Zhao, J.; Trindade, A.C.C.; Liebscher, M.; Silva, F.d.A.; Mechtcherine, V. A review of the role of elevated temperatures on the mechanical properties of fiber-reinforced geopolymer (FRG) composites. *Cem. Concr. Compos.* **2023**, *137*, 104885. [\[CrossRef\]](#)
- Peng, Y.-Q.; Zheng, D.-P.; Pan, H.-S.; Yang, J.-L.; Lin, J.-X.; Lai, H.-M.; Wu, P.-Z.; Zhu, H.-Y. Strain hardening geopolymer composites with hybrid POM and UHMWPE fibers: Analysis of static mechanical properties, economic benefits, and environmental impact. *J. Build. Eng.* **2023**, *76*, 107315. [\[CrossRef\]](#)
- Trindade, A.C.C.; Heravi, A.A.; Curosu, I.; Liebscher, M.; de Andrade Silva, F.; Mechtcherine, V. Tensile behavior of strain-hardening geopolymer composites (SHGC) under impact loading. *Cem. Concr. Compos.* **2020**, *113*, 103703. [\[CrossRef\]](#)
- Kumar, S.; Sekhar Das, C.; Lao, J.; Alrefaei, Y.; Dai, J.-G. Effect of sand content on bond performance of engineered geopolymer composites (EGC) repair material. *Constr. Build. Mater.* **2022**, *328*, 127080. [\[CrossRef\]](#)
- Lin, J.-X.; Chen, G.; Pan, H.-S.; Wang, Y.-C.; Guo, Y.-C.; Jiang, Z.-X. Analysis of stress-strain behavior in engineered geopolymer composites reinforced with hybrid PE-PP fibers: A focus on cracking characteristics. *Compos. Struct.* **2023**, *323*, 117437. [\[CrossRef\]](#)
- Lee, S.K.; Oh, T.; Banthia, N.; Yoo, D.-Y. Optimization of fiber aspect ratio for 90 MPa strain-hardening geopolymer composites (SHGC) with a tensile strain capacity over 7.5%. *Cem. Concr. Compos.* **2023**, *139*, 105055. [\[CrossRef\]](#)
- Lương, Q.-H.; Nguyễn, H.H.; Nguyễn, P.H.; Kang, S.-T.; Lee, B.Y. Extremely-ductile alkali-activated slag-based composite with a tensile strain capacity up to 22%. *Ceram. Int.* **2023**, *49*, 12069–12078. [\[CrossRef\]](#)
- Choi, J.-I.; Lee, B.Y.; Ranade, R.; Li, V.C.; Lee, Y. Ultra-high-ductile behavior of a polyethylene fiber-reinforced alkali-activated slag-based composite. *Cem. Concr. Compos.* **2016**, *70*, 153–158. [\[CrossRef\]](#)
- Ohno, M.; Li, V.C. An integrated design method of Engineered Geopolymer Composite. *Cem. Concr. Compos.* **2018**, *88*, 73–85. [\[CrossRef\]](#)
- Kan, L.; Wang, F. Mechanical properties of high ductile alkali-activated fiber reinforced composites incorporating red mud under different curing conditions. *Ceram. Int.* **2022**, *48*, 1999–2011. [\[CrossRef\]](#)
- Nematollahi, B.; Sanjayan, J.; Qiu, J.; Yang, E.-H. Micromechanics-based investigation of a sustainable ambient temperature cured one-part strain hardening geopolymer composite. *Constr. Build. Mater.* **2017**, *131*, 552–563. [\[CrossRef\]](#)

26. Ling, Y.; Wang, K.; Li, W.; Shi, G.; Lu, P. Effect of slag on the mechanical properties and bond strength of fly ash-based engineered geopolymer composites. *Compos. Part B Eng.* **2019**, *164*, 747–757. [[CrossRef](#)]
27. Nematollahi, B.; Sanjayan, J.; Shaikh, F.U.A. Matrix design of strain hardening fiber reinforced engineered geopolymer composite. *Compos. Part B Eng.* **2016**, *89*, 253–265. [[CrossRef](#)]
28. Zhang, P.; Wei, S.; Zheng, Y.; Wang, F.; Hu, S. Effect of Single and Synergistic Reinforcement of PVA Fiber and Nano-SiO₂ on Workability and Compressive Strength of Geopolymer Composites. *Polymers* **2022**, *14*, 3765. [[CrossRef](#)]
29. Yu, Y.; Yan, H.; Zhu, H.; Chen, J.; Xia, W.; Xu, C.; Song, M. Effect of high strain rate hot compression on the microstructure evolution and subsequent α precipitation of TC17 alloy during single-step and duplex aging. *Mater. Today Commun.* **2023**, *37*, 107041. [[CrossRef](#)]
30. Lee, B.Y.; Cho, C.-G.; Lim, H.-J.; Song, J.-K.; Yang, K.-H.; Li, V.C. Strain hardening fiber reinforced alkali-activated mortar—A feasibility study. *Constr. Build. Mater.* **2012**, *37*, 15–20. [[CrossRef](#)]
31. Ahmed, S.F.U.; Ronnie, Z. Ductile behavior of polyethylene fibre reinforced geopolymer composite. *EDP Sci.* **2017**, *97*, 01047. [[CrossRef](#)]
32. Alrefaei, Y.; Dai, J.-G. Tensile behavior and microstructure of hybrid fiber ambient cured one-part engineered geopolymer composites. *Constr. Build. Mater.* **2018**, *184*, 419–431. [[CrossRef](#)]
33. Khan, M.Z.N.; Hao, Y.; Hao, H.; Shaikh, F.U.A. Experimental evaluation of quasi-static and dynamic compressive properties of ambient-cured high-strength plain and fiber reinforced geopolymer composites. *Constr. Build. Mater.* **2018**, *166*, 482–499. [[CrossRef](#)]
34. Khan, M.Z.N.; Hao, Y.; Hao, H.; Shaikh, F.U.A. Mechanical properties and behaviour of high-strength plain and hybrid-fiber reinforced geopolymer composites under dynamic splitting tension. *Cem. Concr. Compos.* **2019**, *104*, 103343. [[CrossRef](#)]
35. Menna, C.; Asprone, D.; Forni, D.; Roviello, G.; Ricciotti, L.; Ferone, C.; Bozza, A.; Prota, A.; Cadoni, E. Tensile behaviour of geopolymer-based materials under medium and high strain rates. *EPJ Web Conf.* **2015**, *94*, 01034. [[CrossRef](#)]
36. Wang, Y.; Zhong, H.; Zhang, M. Experimental study on static and dynamic properties of fly ash-slag based strain hardening geopolymer composites. *Cem. Concr. Compos.* **2022**, *129*, 104481. [[CrossRef](#)]
37. Pan, H.; Xie, Z.; Chen, G.; Su, J.; Zhuo, K.; Chen, Z.; Lin, J.; Feng, C.; Guo, Y. Dynamic compressive behavior of high-strength engineered geopolymer composites. *J. Build. Eng.* **2023**, *80*, 108036. [[CrossRef](#)]
38. Zhong, H.; Zhang, M. Effect of recycled polymer fibre on dynamic compressive behaviour of engineered geopolymer composites. *Ceram. Int.* **2022**, *48*, 23713–23730. [[CrossRef](#)]
39. Zhong, H.; Zhang, M. Dynamic splitting tensile behaviour of engineered geopolymer composites with hybrid polyvinyl alcohol and recycled tyre polymer fibres. *J. Clean. Prod.* **2022**, *379*, 134779. [[CrossRef](#)]
40. Cai, J.; Pan, J.; Han, J.; Lin, Y.; Sheng, Z. Impact behaviours of engineered geopolymer composite exposed to elevated temperatures. *Constr. Build. Mater.* **2021**, *312*, 125421. [[CrossRef](#)]
41. Cai, J.; Pan, J.; Han, J.; Lin, Y.; Sheng, Z. Low-energy impact behavior of ambient cured engineered geopolymer composites. *Ceram. Int.* **2022**, *48*, 9378–9389. [[CrossRef](#)]
42. GB/T 18046-2017; Ground Granulated Blast Furnace Slag Used for Cement and Concrete. Standard of the People's Republic of China: Beijing, China, 2017.
43. Li, Q.; Wang, J.; Zhou, Z.; Du, P.; Zhang, X. Effect of BaCl₂ on the hydration properties of ultrahigh performance geopolymer concrete. *Constr. Build. Mater.* **2023**, *403*, 133074. [[CrossRef](#)]
44. ASTM-C1437; Flow of Hydraulic Cement Mortar. Annual Book of ASTM Standards: Philadelphia, PA, USA, 2013.
45. Yokota, H.; Rokugo, K.; Sakata, N. JSCE recommendations for design and construction of high performance fiber reinforced cement composite with multiple fine cracks. In Proceedings of the High Performance Fiber Reinforced Cement Composites, Tokyo, Japan, 1 June 2008.
46. ASTM-C39/C39M; Standard Test Method for Compressive Strength of Cylindrical Concrete Specimens. Annual Book of ASTM Standards: Philadelphia, PA, USA, 2023.
47. ASTM-C469/C469M; Static Modulus of Elasticity and Poisson's Ratio of Concrete in Compression. Annual Book of ASTM Standards: Philadelphia, PA, USA, 2014.
48. Lin, J.-X.; Su, J.-Y.; Pan, H.-S.; Peng, Y.-Q.; Guo, Y.-C.; Chen, W.-S.; Sun, X.-L.; Yuan, B.-X.; Liu, G.-T.; Lan, X.-W. Dynamic compression behavior of ultra-high performance concrete with hybrid polyoxymethylene fiber and steel fiber. *J. Mater. Res. Technol.* **2022**, *20*, 4473–4486. [[CrossRef](#)]
49. Zhao, H.; Gary, G. A new method for the separation of waves. Application to the SHPB technique for an unlimited duration of measurement. *J. Mech. Phys. Solids* **1997**, *45*, 1185–1202. [[CrossRef](#)]
50. Hu, C.-F.; Li, L.; Li, Z. Effect of fiber factor on the workability and mechanical properties of polyethylene fiber-reinforced high toughness geopolymers. *Ceram. Int.* **2022**, *48*, 10458–10471. [[CrossRef](#)]
51. Bai, T.; Liu, B.; Wu, Y.; Huang, W.; Wang, H.; Xia, Z. Mechanical properties of metakaolin-based geopolymer with glass fiber reinforcement and vibration preparation. *J. Non-Cryst. Solids* **2020**, *544*, 120173. [[CrossRef](#)]
52. Ranjbar, N.; Mehrali, M.; Mehrali, M.; Alengaram, U.J.; Jumaat, M.Z. Graphene nanoplatelet-fly ash based geopolymer composites. *Cem. Concr. Res.* **2015**, *76*, 222–231. [[CrossRef](#)]
53. Wang, Y.; Liu, F.; Yu, J.; Dong, F.; Ye, J. Effect of polyethylene fiber content on physical and mechanical properties of engineered cementitious composites. *Constr. Build. Mater.* **2020**, *251*, 118917. [[CrossRef](#)]

54. Vilaplana, J.L.; Baeza, F.J.; Galao, O.; Alcocel, E.G.; Zornoza, E.; Garcés, P. Mechanical properties of alkali activated blast furnace slag pastes reinforced with carbon fibers. *Constr. Build. Mater.* **2016**, *116*, 63–71. [[CrossRef](#)]
55. Xiao, S.-H.; Liao, S.-J.; Zhong, G.-Q.; Guo, Y.-C.; Lin, J.-X.; Xie, Z.-H.; Song, Y. Dynamic properties of PVA short fiber reinforced low-calcium fly ash—Slag geopolymer under an SHPB impact load. *J. Build. Eng.* **2021**, *44*, 103220. [[CrossRef](#)]
56. Chen, Z.; Yang, Y.; Yao, Y. Quasi-static and dynamic compressive mechanical properties of engineered cementitious composite incorporating ground granulated blast furnace slag. *Mater. Des.* **2013**, *44*, 500–508. [[CrossRef](#)]
57. Yu, Q.; Zhuang, W.; Shi, C. Research progress on the dynamic compressive properties of ultra-high performance concrete under high strain rates. *Cem. Concr. Compos.* **2021**, *124*, 104258. [[CrossRef](#)]
58. Chen, M.; Chen, W.; Zhong, H.; Chi, D.; Wang, Y.; Zhang, M. Experimental study on dynamic compressive behaviour of recycled tyre polymer fibre reinforced concrete. *Cem. Concr. Compos.* **2019**, *98*, 95–112. [[CrossRef](#)]
59. joo Kim, D.; Sirijaroonchai, K.; El-Tawil, S.; Naaman, A.E. Numerical simulation of the Split Hopkinson Pressure Bar test technique for concrete under compression. *Int. J. Impact Eng.* **2010**, *37*, 141–149. [[CrossRef](#)]
60. Georgin, J.F.; Reynouard, J.M. Modeling of structures subjected to impact: Concrete behaviour under high strain rate. *Cem. Concr. Compos.* **2003**, *25*, 131–143. [[CrossRef](#)]
61. Cotsovos, D.M.; Pavlović, M.N. Numerical investigation of RC structural walls subjected to cyclic loading. *Comput. Concr.* **2005**, *2*, 215–238. [[CrossRef](#)]
62. Zhang, D.; Tu, H.; Li, Y.; Weng, Y. Effect of fiber content and fiber length on the dynamic compressive properties of strain-hardening ultra-high performance concrete. *Constr. Build. Mater.* **2022**, *328*, 127024. [[CrossRef](#)]
63. Li, N.; Jin, Z.; Long, G.; Chen, L.; Fu, Q.; Yu, Y.; Zhang, X.; Xiong, C. Impact resistance of steel fiber-reinforced self-compacting concrete (SCC) at high strain rates. *J. Build. Eng.* **2021**, *38*, 102212. [[CrossRef](#)]
64. Comite Euro-International Du Beton. *CEB-FIP Model Code 1990*; Comite Euro-International Du Beton Thomas Telford Publishing: London, UK, 1991; pp. 87–109.
65. Grote, D.L.; Park, S.W.; Zhou, M. Dynamic behavior of concrete at high strain rates and pressures: I. experimental characterization. *Int. J. Impact Eng.* **2001**, *25*, 869–886. [[CrossRef](#)]

Disclaimer/Publisher’s Note: The statements, opinions and data contained in all publications are solely those of the individual author(s) and contributor(s) and not of MDPI and/or the editor(s). MDPI and/or the editor(s) disclaim responsibility for any injury to people or property resulting from any ideas, methods, instructions or products referred to in the content.